13th IEA Heat Pump Conference
April 26-29, 2021 Jeju, Korea

Frosting and Defrosting Behavior of Evaporators

Christoph Reichl[a,*], Mirza Popovac[a], Felix Hochwallner[a], Peter Wimberger[b], Felix Linhardt[a,b], Thomas Fleckl[a], Johann Emhofer[a]

[a]Austrian Institute of Technology GmbH, Center for Energy, Vienna 1210, Austria
[b]Vienna University of Technology, Institute of Applied Physics, Vienna 1040, Austria

Abstract

Air-to-water heat pumps - being essential to reach the ambitious climate goals – don't come without challenges: Evaporators of air-to-water heat pumps are prone to severe frosting in humid climatic during late fall, winter and spring. To sustain a reasonable CoP, de-frosting strategies are employed to remove the frost layer and restore normal operation. De-frosting, however, also reduces efficiency due to downtimes and heat loss due to reverse operation. Frosting and de-frosting of evaporators is characterized using overview and detailed image capturing. The frost growth is additionally quantitatively assessed using a digital high-resolution scale. Together with the thermodynamic data of the heat pump and the control parameters of the climatic chamber a full transient data set is available and analysed deriving frosting and de-frosting correlations. The extensive data set is an important base for numerical simulation: Frost growth and weight increase can be used to validate three-dimensional frosting models necessary to simulate and - in a second stage - optimize evaporator designs. Furthermore, the thermodynamic behaviour during frosting and de-frosting is an important input to one-dimensional system models of heat pumps.

Selection and/or peer-review under responsibility of the organizers of the 13th IEA Heat Pump Conference 2020.

Keywords: frosting; de-frosting; evaporator; image processing

1. Introduction

The frosting of heat exchangers is typically undesired in heat pump operation, given that in most of the cases it implies a deterioration of the equipment performance or even critical safety problems. In that view, the understanding of the factors affecting the frosting process is of high practical relevance, and a large research community is involved in the investigation of the frosting behaviour.

Empirical correlations for the relevant frost characteristics (respectively, frost density and conductivity, mass diffusivity and latent heat of sublimation) have been presented by [1], [2] and [3], among others. This is accompanied by comprehensive numerical work to provide the theoretical background: In a series of studies, Na and Webb [4], [5] presented their work on the frost formation over simple geometrical configurations, successfully reproducing the experimental frosting results. Focusing on the reduction of the computational cost, [6] proposed an algebraic approach for the frost growth and densification. [7] advanced the psychometric and surface conditions under which the frost formation occurs.

Comprehensive reviews are available on frosting of air-to-air heat exchangers (see [8], [9]) and the frost deposition on flat surfaces [10]. Different surface structures have been investigated [11], [12]. Heat transfer characteristics under frosting and defrosting are discussed in [13] and have been put in the general context of building applications by [14].

* Corresponding author. Tel.: +43-50550-6605; fax: +43-50550-6649
E-mail address: christoph.reichl@ait.ac.at

In this paper time dependent frosting of the heat exchanger has been observed in the SilentAirHP heat pump assembly by measuring the mass increase and using postprocessing of captured images of the heat exchanger during frosting for different environmental conditions. In section 2 we will describe the experimental heat pump setup. This is followed by a discussion of the experimental methods used to characterize frosting on the evaporator in section 3. In section 4 we are going to present and discuss the experimental results. We will conclude this work by summarizing our experimental approaches and presenting an overview of planned future work.

2. Experimental Heat Pump and Evaporator Component

For our measurements we used an experimental air-source heat pump (see Figure 1) which was designed to provide a heating power of 5 kW at a heating water temperature of 35°C and at an ambient air temperature of 2°C. The refrigerant R410A was used and the entire heat pump was located inside the AIT climatic chambers during the measurements. Inside the chamber, the air temperature and humidity could be controlled. The heating water was cooled with an in-house chilled water reservoir with the back flow of the heating water regulated to 30°C. The compressor was operated at a fixed rotational speed of 98Hz. The superheating was always set to 7°C during the experiments. The fan operated at a constant rotational speed what corresponds to an average velocity of 2 m/s at the fin and tube evaporator. The dimensions of the evaporator are 630 mm x 560 mm with a depth of 120 mm. The fins are made of corrugated aluminium and placed in a distance of 4 mm. 78 horizontal tubes made of smooth copper are organized in 4 columns in air flow direction. The overall pressure drop of the evaporator is about 54 Pa, if dry. The condenser has been realized as a plate condenser designed for a heating capacity of 5 kW at an outside air temperature of 2°C and a supply temperature of 35°C and a condensation temperature of 40°C.

3. Measurement methods

Alongside the acquisition of thermodynamic data of both the heat pump and climatic chamber, transient weight measurements and image capturing techniques have been used.

3.1. Heat Pump and Climatic Chamber Thermodynamics

The temperatures at the refrigerant inlet and outlet of the evaporator were measured with calibrated PT100-class A temperature sensors. The sensors were mounted with heat-conductive paste on the outside of the copper pipes as close to the inlet as possible. Furthermore, the sensors were insulated to reduce heat exchange with the ambient air. The climatic conditions in the chamber are measured with several combined temperature and humidity sensors placed at the suction side of the heat exchanger according to the standards normally used for heat pump certification tests (EN14511-3:2018) [15]. An additional temperature and humidity sensor is placed at the suction side for climate chamber control.

3.2. Transient Weight Measurements

The heat pump assembly has been placed on a scale capable of measuring the weight as a function of time. By calculating the difference between the increasing weight and the initial weight, the amount of frost on the heat exchanger can be extracted. As the weight of the heat pump assembly was by a factor of 1.5 higher than the maximum detectable load of the scales, a balance construction was put in place and the system was calibrated by subsequently placing known weights on the dry heat exchanger and recording a calibration curve before starting the frosting experiments.

We selected a setup with an air inflow temperature of 2°C with quite small defrosting cycle times for better visualization of the procedure. Figure 3 shows the measured mass signal on the left side. As a next step each frosting cycle is identified (shown in Figure 3 right side marked with a unique colour). As the final step, the mass signals of the different frosting cycles are superimposed (see Figure 4) and a mean mass signal is derived which can then be used for comparison to numerical data (see also Figure 11).

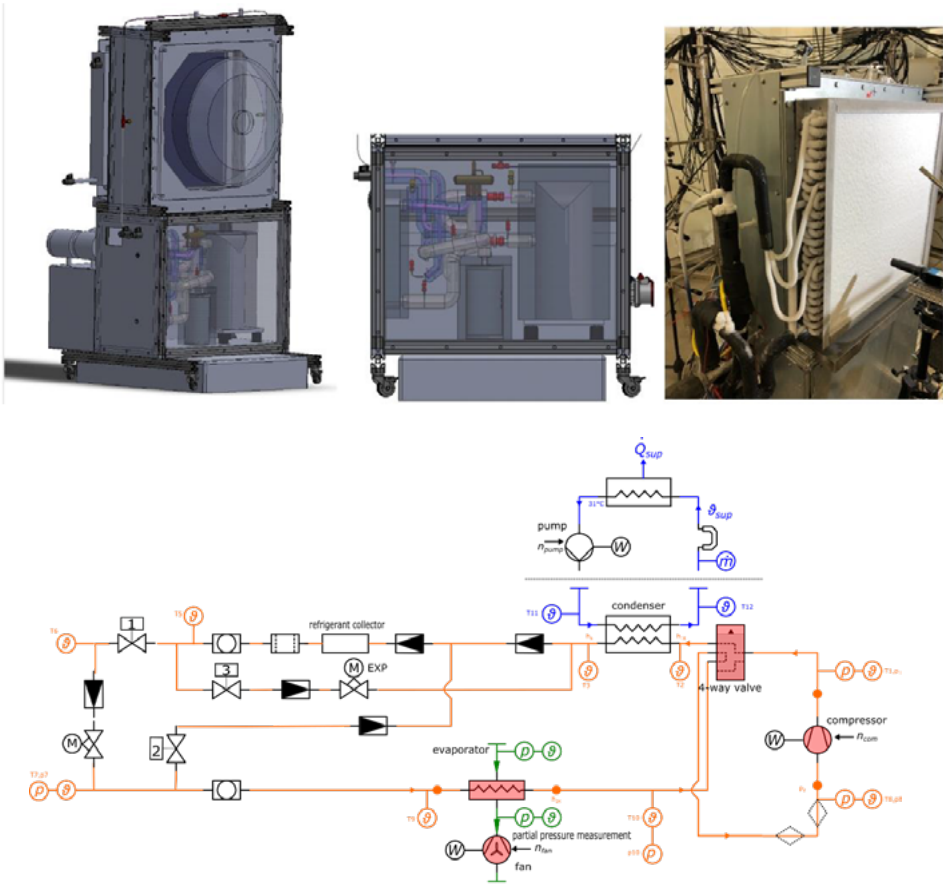

Fig. 1. (top left) Sketch of the experimental SilentAirHP heat pump showing the major components; (top middle) lower part of the SilentAirHP with compressor, condenser, expansion valve and duct network; (top right) SilentAirHP evaporator fully covered with ice in the climatic chamber of AIT. (bottom): sketch of the heat pump design with sensor positions.

3.3. Image Capturing and Highlight Event Extraction

Two cameras have been used to capture the frosting of the heat exchanger. A thermal-camera capable of recording thermographic stills and standard image stills at the same time and a macro camera recording a detailed view of a part of the heat exchanger used for highlight event extraction. For the standard images both, a normal view and a differential view between the actual image and an image recorded in the initial state (without frost) is shown: an example of the detailed view is given in Figure 2 on the right side; the total view is given on the left side. The setup of the cameras can also be seen in Figure 5.

In order to quantify the frost accumulation, the scale signal and the amount of pixel exceeding a certain brightness threshold in the pictures may be used. A pixel exceeds the brightness threshold if the mean of the red, green and blue value is higher than 200. At the beginning only the pixels displaying the metallic surface of the fins will exceed this brightness threshold. But as soon as frost is accumulating, additional pixel will exceed this threshold. Pixels exceeding the stated threshold (“white” pixels) are from now flagged as highlight events for additional processing.

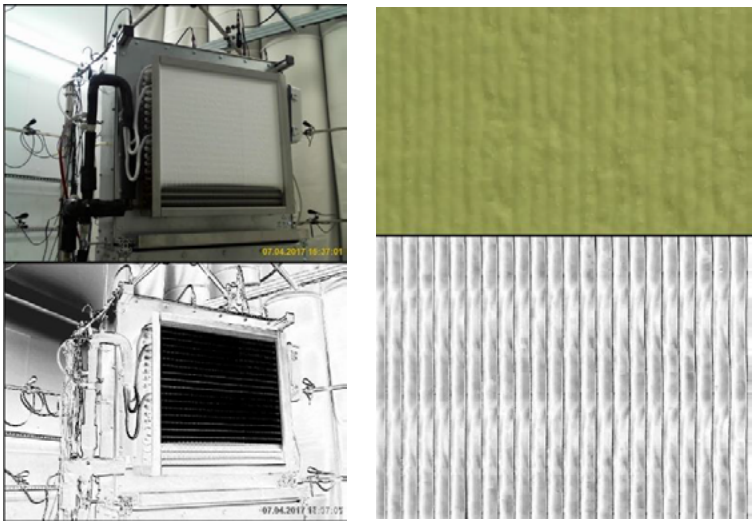

Fig. 2. Measurement overview with full frosting. The humidity in the climatic chamber has been increased to its maximum reachable value to reach full frost state. Left side: full image of the heat pump showing severe frosting on the top and a differential image of the heat exchanger showing frost only on the bottom; Right side: detailed view on the heat exchanger fins with full frosting on top and differential image of detailed view on the frosting heat exchanger showing frost only on the bottom.

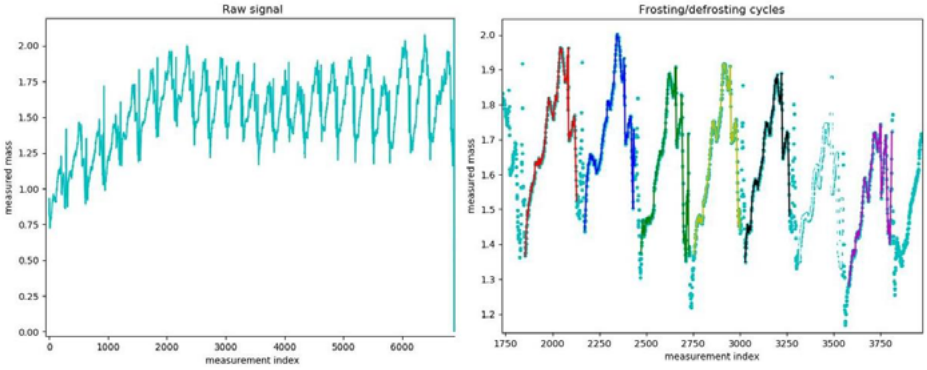

Fig. 3. (left) Measured mass given in kg shown as function of the measurement index for an inflow air temperature of 2°C; (right) Frost mass versus measurement index for a section of the whole measurement period (shown on left side). Each frosting cycle is identified by visual inspection and marked with a unique colour for visualization.

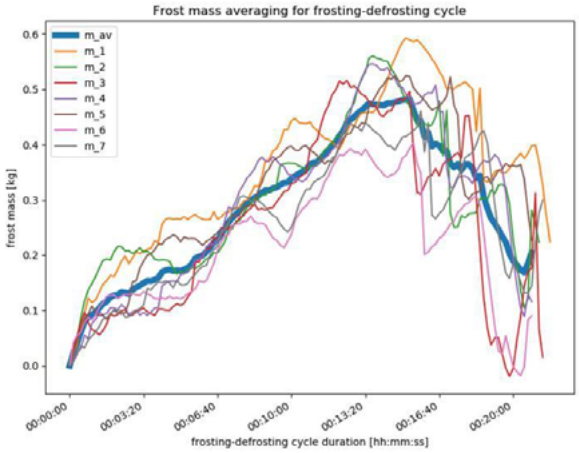

Fig. 4. Frost mass given in kg as a function of frosting-defrosting duration. The single repetitive events shown in Fig. 3 right are now superimposed to allow for the generation of a mean average frosting cycle and presented via the time duration.

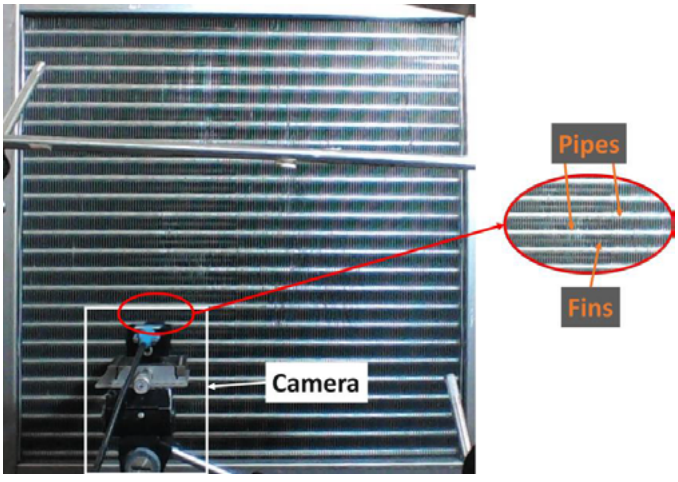

Fig. 5. Surface of the SilentAirHP heat exchanger and macro camera used to visualize the frost accumulation on the heat exchanger fins.

4. Experimental Results and Discussion

A common webcam can also be used to visualize the nonuniform frost accumulation on the heat exchanger surface (see Figure 6). It can be seen, that the frost is not forming uniformly on the whole heat exchanger surface, but rather patchy. The camera with the macro lenses used to visualize the frost growth between two fins is located at a representative area, where the frost growth is clearly visible. The rod looming over the pictures is a humidity sensor.

The macro camera was used to give a detailed view of the frost accumulation and dissipation on one or two fins of the heat exchanger. In Figure 5 the surface of the SilentAirHP heat exchanger and the macro camera used to visualize the frost accumulation on the heat exchanger fins is shown. The boundary conditions for the frosting behaviour analysis of the SilentAirHP are listed in Table 1. The pictures of the frost accumulation

between two fins can be seen in Figure 7. In Figure 8 the scale measurements and the amount of highlight events is shown over time.

Table 1. Operation and ambient conditions for the analysis of the frosting behaviour of the SilentAirHP.

θ_{amb}	RH_{amb}	η_{comp}	η_{fan}	Refrigerant	Fin type	Coating	Fin area
6.3°C	71.8%	94 Hz	99 Hz	R410A	Straight flat fins	Clearcoat U-Sil 120 GL	11.44 m^2

Legend:
θ_{amb} … Ambient temperature // RH_{amb} … Relative Humidty // η_{comp} … Rotational frequency of the compressor
η_{fan} … Rotational frequency of the fan // Refrigerant … Used refrigerant // Fin type … Fin type used for the reported measurement
Coating … Coating used for surface treatment of the fins // Fin area … Total area of the fins

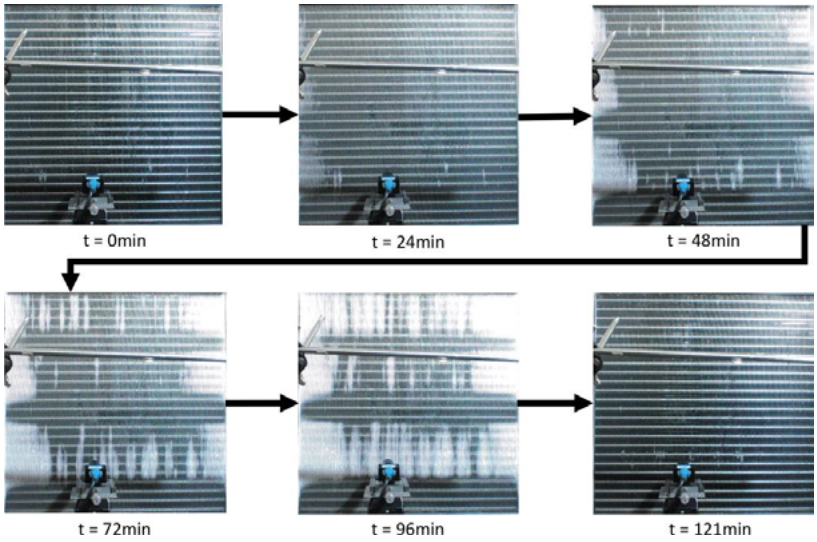

Fig. 6. Nonuniform frost formation on the heat exchanger surface of the SilentAirHP.

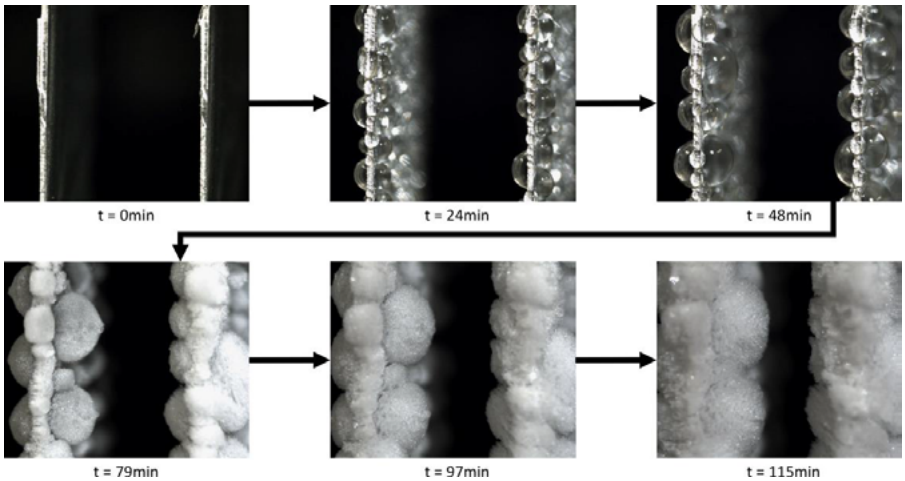

Fig. 7. Frost accumulation on two fins of the coated evaporator of the SilentAirHP for operation and ambient conditions as defined in Table 1.

Frosting of the SilentAirHP starts with small water drops condensing on the surface of the vertical fins. The water drops start fusing together forming bigger water drops. These bigger water drops start to freeze, building frost globes on the fins of the heat exchanger. Advancing in time, the frost globes start fusing together and the frost continues to densify. When the frost layer is too thick, the SilentAirHP starts to defrost, in order to assure continues stable operation. This defrosting is done by reversing the cycle via a four-way valve.

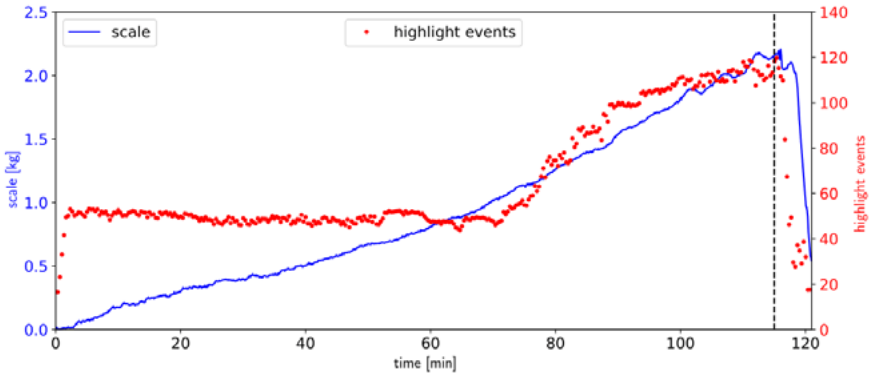

Fig. 8. Scale measurement and amount of highlight events in pictures of the SilentAirHP during frosting conditions and defrosting operation. The time when defrosting is initiated is marked with a dotted line.

After reversing the cycle, the frosted heat exchanger, which acted as the evaporator for the refrigerant, afterwards works as the condenser for the refrigerant, transferring heat to the outlet air and to the frost on its fins. Defrosting of the heat exchanger is done in a very short period of time. The defrosting of the SilentAirHP can be seen in Figure 9.

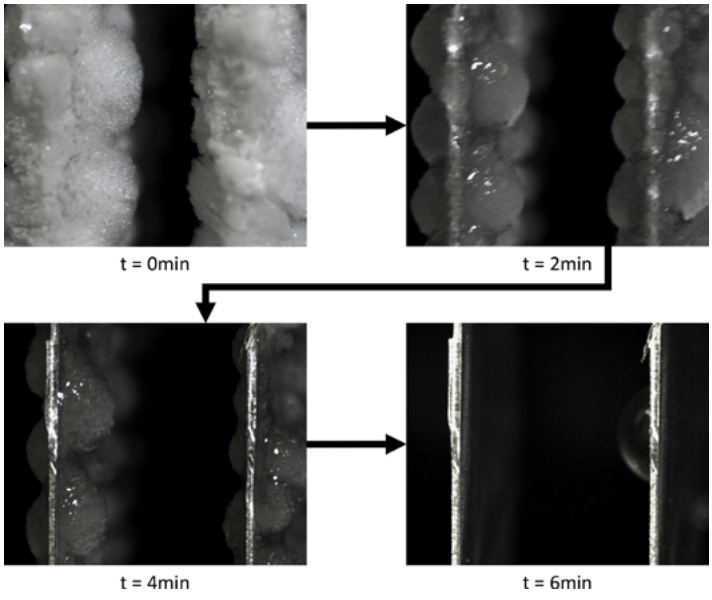

Fig. 9. Defrosting of the coated evaporator of the SilentAirHP for operation and ambient conditions as defined in Table 1.

Defrosting of the SilentAirHP takes only 6 min, while the operation at frosting conditions was able to be operated in an almost stable manner for 115 minutes for the settings given in Table 1. Therefore, the heat pump can be operated in regular heating mode for approximately 95% of the time at these conditions. When the ice layer is formed on the evaporator surface, however, the heat pump performance begins to decrease slightly. This can also be seen in the temperature sensors placed inside the heat pump (see Fig. 12). When the frost layer grows starting around 70 minutes (see Fig. 8), the valve, compressor and condenser temperatures both on the discharge and suction side begin to fall slightly indicating this decrease in performance.

During the remaining 5% of the time the heat exchanger has to be defrosted. When defrosting is started, the fins rapidly take the hot temperature of the refrigerant. Therefore, the frost is melted from its surface, forming liquid water which flows down the vertical fins. This water flows down the heat exchanger until it reaches the ground it stands on. In Figure 8 the scale measurements and the amount of highlight events in the pictures during frosting and defrosting operation of the SilentAirHP is shown. The mass on the heat exchanger is constantly rising, due to condensing water on the heat exchanger fins and afterwards frosting of the water drops and densifying of the frost. During the first 70 minutes nearly no change in highlight events is visible, as the condensed water drops do not count as highlight events, but only frost does. After 70 minutes the amount of highlight events is increasing. Just after beginning of defrost operation, which is marked with a dotted line in the plot, the amount of highlight events and the mass of the scale is decreasing rapidly, as the frost is melting, and the water drains off. It is interesting to compare the close-up view (Figure 7) with the global view (Figure 6): On the first and last picture in the global view, where the close up camera suggests complete termination of the defrosting operation, falling water drops are still visible on the webcam pictures.

Frosting cycles have been measured for several environmental conditions defined by the evaporator air inflow temperature. The climate chamber was set to a sustain a defined relative humidity. This can only be achieved with some fluctuations especially in the vicinity of defrosting. For and outdoor air temperature of 2°C, 4.5°C and 7°C, a relative humidity of 87.3%, 86.4% and 78%, respectively was measured. During defrosting, however, the relative humidity in the chamber cannot be sustained by the climate chamber control and deviates from this number. After defrosting the humidity control of the climate chamber is able to bring the conditions back. The relative mass signals are shown in Figure 10 for air inflow temperatures of 2.0°C, 4.5°C and 7.0°C. The average frost mass for these different air inflow temperatures is shown in Figure 11. It can clearly be seen, that the implemented control algorithm acts differently for the different situations. Cycle times for the 7°C air inflow temperature are - with around 120 min - longer than those for an air inflow temperature of 4.5°C which lie around 80 minutes. Not only the amount of accumulated frost is different – also the shape of the weight increase curves shows a different behaviour – not only in curvature but also in their repetitiveness. The employed control algorithm leads to very frequent defrosting for the 2°C air inflow temperature setting.

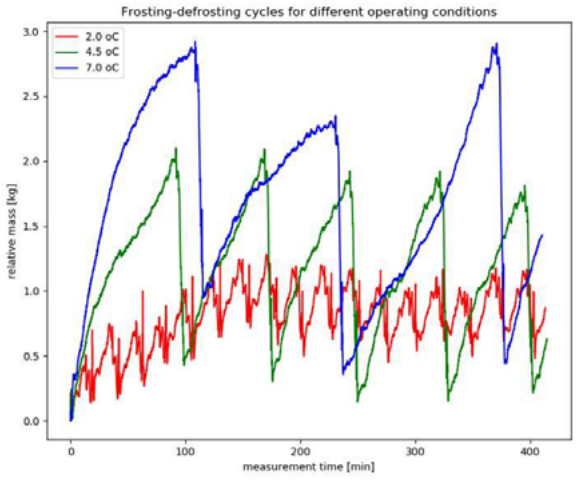

Fig. 10. Frost mass given as a function of the measurement time for three different temperatures (given in °C) of the inflow air. In all cases, several frosting/defrosting cycles are shown.

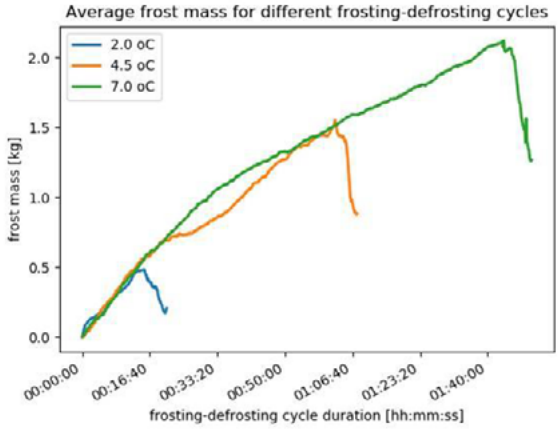

Fig. 11. Average frost mass given as a function of the measurement time for three different temperatures (given in °C) of the inflow air.

Defrosting of the heat pump was triggered once the evaporator pressure (which is equivalent to an evaporation temperature) has fallen below a certain lower limit. This is an indication for a decreased heat transfer through the evaporator what goes hand in hand with an increased frost thickness and a lower COP. Since, the defrost condition was not corelated to the outdoor temperature condition in our experiments, the time before defrosting increases for higher outdoor temperatures. This fact is also reflected in the differences in frost aggregation (mass uptake, see Figure 11).

The refrigerant temperatures during operation are shown in Figure 12 for the settings given in Table 1. During operation of the heat pump at frosting conditions most refrigerant temperatures fluctuate but the mean of most temperatures stay approximately constant. However, about thirty minutes before defrosting the mean of some refrigerant temperatures, as well as the compressor suction and discharge temperatures, decrease slightly. When defrosting is initiated the compressor discharge temperature, the valve suction temperature, the condenser suction temperature and the condenser discharge temperature fall significantly. Meanwhile, the compressor suction and the valve discharge temperature rise. This operation mode is maintained only for a very short time and the temperatures are fluctuating heavily during this mode.

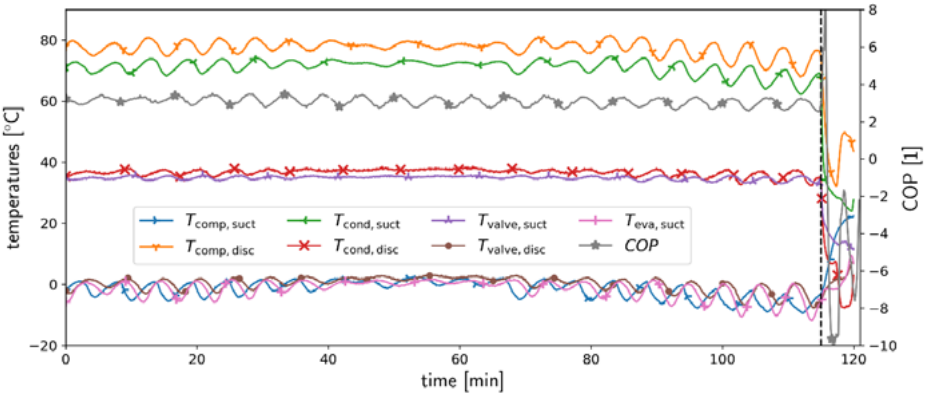

Fig. 12. Development of the refrigerant temperatures over time during operation of the SilentAirHP at frosting conditions. The time when defrosting is initiated is marked with a black dotted line. The CoP is added as a grey curve.

5. Conclusions and Outlook

Frosting of evaporators is commonly observed especially in mild climates and a defrosting procedure has to be put in place allow for a continuous operation of the heat pump. The evaporator, however, is only one part of the complete setup: Frosting of the fins and tubes and hence subsequent blocking of the evaporator leads to an increased pressure drop over the evaporator which could force the fan to run in a different operating point. Furthermore, the frost layer changes the heat transfer characteristics of the evaporator.

In this paper we introduced methods for measuring the weight increase using scales and visualizing ice accretion using postprocessing of images captured from the evaporator surface during heat pump operation. We could show, that there is a good correlation between the weight increase and the number of highlight events present in the images captured. Furthermore, the formation of droplets on the fin structures and subsequently freezing eventually building up an ice layer between the fins could be shown with a macro camera providing very detailed images. It should be noted, that selecting the right spot for the macro camera is important to achieve representative ice accretion data.

The experimental characterization methodologies built around the experimental heat pump "SilentAirHP" proved to be a robust testbed for identification of efficient ways to detect frosting states, which will be used to derive soft sensors in the framework of the IoT (Internet of Things) heat pump initiative. The test-rig using full control capabilities of the self-made heat pump is further capable of comparing different evaporators and/or evaporators with different coatings.

Finally, the data base available through the frosting and defrosting experiments is key to validate numerical simulations performed to simulate the frosting process either on full evaporator geometries or smaller symmetric elements used to reconstruct the behaviour of the full evaporator setups. The images from the macro camera visualize the frosting process and can be used to compare to very high detailed simulation results. The numerical approaches allow for assisting in evaporator design and development.

Acknowledgements

The Austrian Research Promotion Agency (FFG) and the Austrian Climate and Energy Fund (KLIEN) is gratefully acknowledged for funding this work under Grant No. 848891 (program line 'Energieforschung e!Mission 1st call', project 'SilentAirHP'). Part of the work has been performed within the 7th Framework Programme (FP7) European Commission grant agreement No FP7-Energy-2012-308816.

References

[1] Y. Hayashi, A. Aoki, S. Adashi, K. Hori, Study of frost properties correlating with frost formation types, *ASME J. Heat Transfer* **99** (1977) 239245.

[2] H. R. Pruppacher, J. D. Klett, Microphysics of Clouds and Precipitation, Reidel, Dordrecht, 1978.

[3] P. G. Mago, S. A. Sheriff, Frost formation and heat transfer on a cold surface in ice fog, *AIAA-2004-164*.

[4] B. Na, R. Webb, A fundamental understanding of factors affecting frost nucleation, *Int. J. Heat Mass Transfe*r **46** (2003) 3797 3808.

[5] B. Na, R. Webb, Mass transfer on and within a frost layer, *Int. J. Heat Mass Transfer* **47** (2004) 899911.

[6] C. J. L. Hermes, R. O. Piucco, J. R. B. Jr., C. Melo, A study of frost growth and densification on flat surfaces, *Experimental Thermal and Fluid Science* **33** (2009) 371-379.

[7] R. O. Piucco, C. J. L. Hermes, C. Melo, J. R. B. Jr., A study of frost nucleation on at surfaces, *Experimental Thermal and Fluid Science* **32** (2008) 17101715.

[8] M. R. Nasr, M. Fauchoux, R. W. Besant, C. J. Simonson, A review of frosting in air-to-air energy exchangers, *Renewable and Sustainable Energy Reviews* **30** (2014) 538-554. doi:https://doi.org/10.1016/j.rser.2013.10.038. URL http://www.sciencedirect.com/science/article/pii/S1364032113007375

[9] Z. Qi, Water retention and drainage on air side of heat exchangers - a review, Renewable and Sustainable *Energy Reviews* **28** (2013) 1-10. doi:https://doi.org/10.1016/j.rser.2013.07.014. URL http://www.sciencedirect.com/science/article/pii/S1364032113004590

[10] A. Loni, M. Mondot, F. Durier, R. Revellin, P. Haberschill, State-of-the-art review of frost deposition on flat surfaces, *International Journal of Refrigeration* **68** (2016) 198-217. doi:https://doi.org/10.1016/j.ijrefrig.2016.04.004.

URL http://www.sciencedirect.com/science/article/pii/S0140700716300457

[11] P. Ganesan, S. Vanaki, K. Thoo, W. Chin, Air-side heat transfer characteristics of hydrophobic and super-hydrophobic fin surfaces in heat exchangers: A review, *International Communications in Heat and Mass Transfer* **74** (2016) 27-35.doi:https://doi.org/10.1016/j.icheatmasstransfer.2016.02.017.
URL http://www.sciencedirect.com/science/article/pii/S0735193316300549

[12] M.-H. Kim, H. Kim, K.-S. Lee, D. R. Kim, Frosting characteristics on hydrophobic and superhydrophobic surfaces: A review, *Energy Conversion and Management* **138** (2017) 1-11.
doi:https://doi.org/10.1016/j.enconman.2017.01.067.
URL http://www.sciencedirect.com/science/article/pii/S0196890417300833

[13] M. S. Patil, J.-H. Seo, M.-Y. Lee, Heat transfer characteristics of the heat exchangers for refrigeration, air conditioning and heat pump systems under frosting, defrosting and dry/wet conditions - a review, *Applied Thermal Engineering* **113** (2017) 1071-1087.
doi:https://doi.org/10.1016/j.applthermaleng.2016.11.107.
URL http://www.sciencedirect.com/science/article/pii/S1359431116332847

[14] C. Zeng, S. Liu, A. Shukla, A review on the air-to-air heat and mass exchanger technologies for building applications, *Renewable and Sustainable Energy Reviews* **75** (2017) 753-774.
doi:https://doi.org/10.1016/j.rser.2016.11.052.
URL http://www.sciencedirect.com/science/article/pii/S1364032116308127

[15] EN14511-3:2018, Air conditioners, liquid chilling packages and heat pumps for space heating and cooling and process chillers, with electrically driven compressors Part 3: Test methods